ESD-TR-89-222

CdTe Buffered GaAs Thin-Slab IR Waveguide Modulators and T/R Filter

P.K. Cheo
R.T. Brown
G. Carrier
W. Glueck
R. Wagner
M. Gilden

Prepared by

United Technologies
Research Center

Prepared for

MIT Lincoln Laboratory
Lexington, Massachusetts

July 1989

UTRC Technical Report R89-927784
Purchase Order No. BX-1404
Prime Contract No. F19628-85-C-0002

2.0 – PERFORMANCE EVALUATION OF CdTe Buffered GaAs WAVEGUIDE MODULATORS

2.1 Definitions

The sideband power, P_s, that can be converted to either the upper or the lower sideband from the laser carrier, is proportional to the laser input power P_ℓ and the microwave driver power P_d as defined by

$$P_s = \eta \, T \, P_\ell \, P_d$$

where η is the single sideband electrooptic conversion efficiency per one watt of modulator drive power, and T is the percent laser power transmitted through the modulator. The explicit expression for η has been derived and given in Ref. 4. The values of both η and T, as well as the laser output beam profile are dependent on the structure parameters of the modulator, which are depicted in Fig. 1, for a CdTe buffered GaAs thin-slab waveguide modulator developed under the Contract (PO BX-1404).

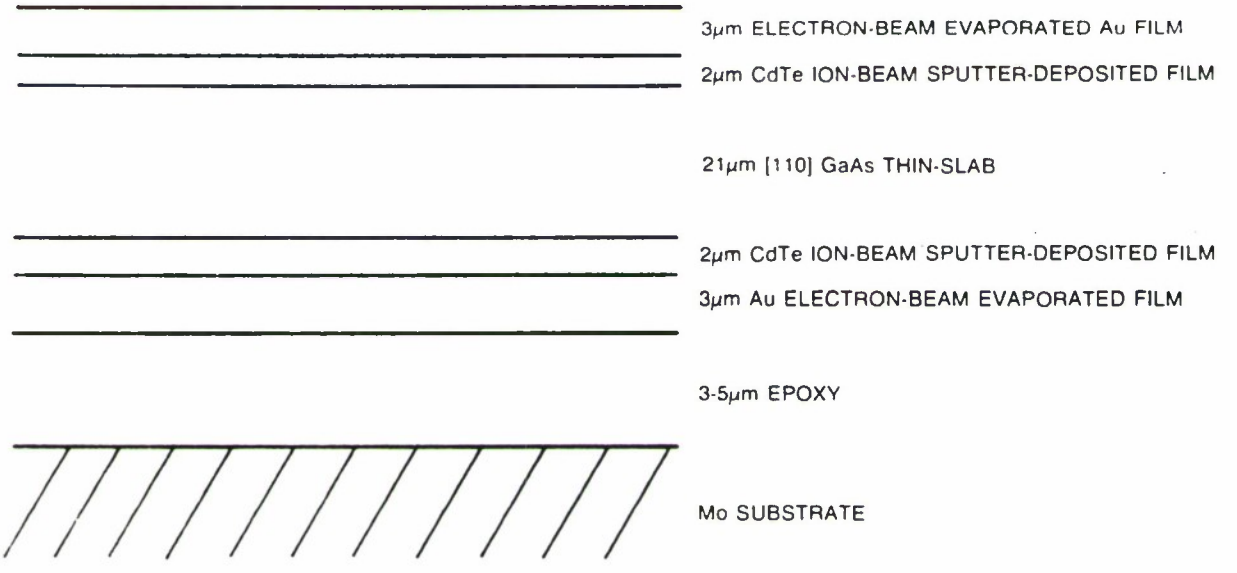

Figure 1. Cross-Section of CdTe Buffered GaAs Thin-Slab Waveguide Modulator

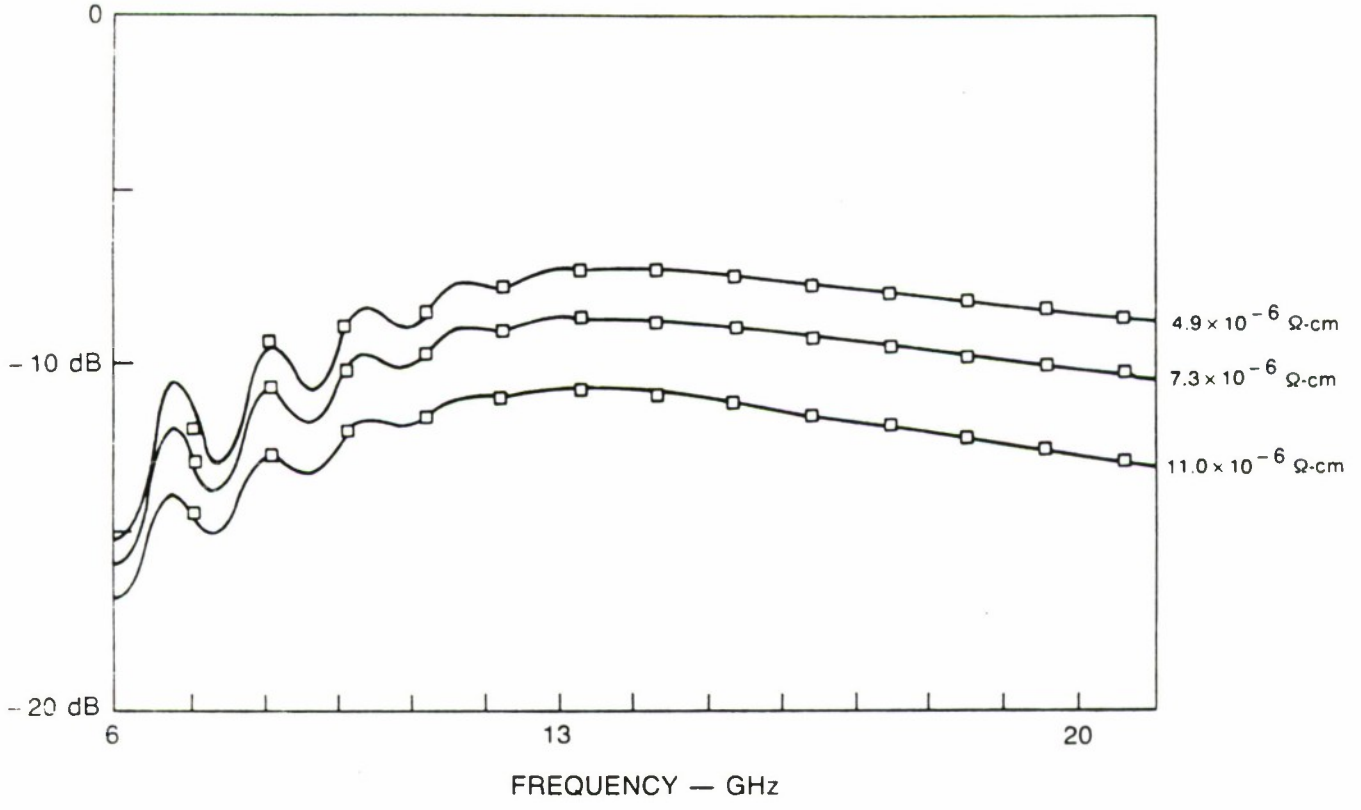

Figure 4. Microstrip Electrode Loss Calculation

It is worth noting that the metal losses dominate the microwave insertion loss which is primarily due to metal absorption. This is supported by the characteristic downward slope of the insertion loss with frequency. The computer model contains some inaccuracies in the transformer sections, however, this uncertainty mainly affects the reflection coefficient instead of the insertion loss.

Initial microwave insertion loss measurements indicated that the microstrip electrodes had very high resistivity values as compared to that of the bulk metal. These microstrip electrodes were made of Cu and Au films (3 μm thick) by ion-beam sputter-deposition. To understand the loss mechanism, a technique was established to obtain direct resistivity measurements for these films at microwave frequencies of interest. Results obtained with this technique indicated that the resistivity of metal films made by ion-beam deposition is much higher (typically 3 to 6 times) than the bulk values, whereas the resistivity of the films prepared by electron beam or thermal evaporation is very close to that of the bulk value. The measured microstrip resistivity value for the buffered modulator delivered to Lincoln Laboratory is 4.4. x 10^{-6} Ω - cm , which is about 1.8 times the bulk resistivity value for gold (2.44 x 10^{-6} Ω - cm). The measured insertion loss versus modulation frequency is plotted in Fig. 5, which shows a relatively flat frequency response ranging from 8 to 18 GHz, at a value of approximately -7.5 dB, consistent with the calculation.

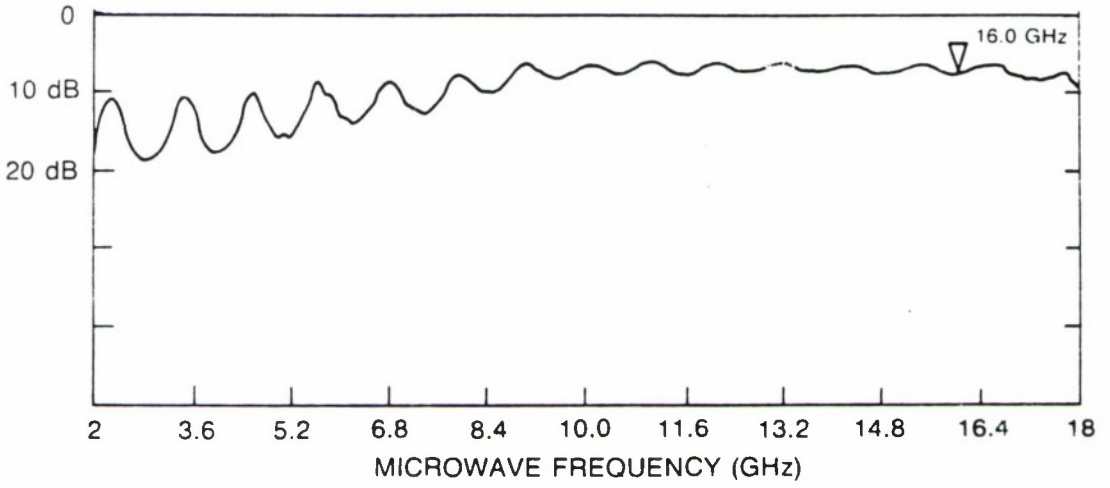

Figure 5. Microstrip Insertion Loss Measurement

2.4 Sideband Power Conversion Efficiency

To measure the sideband power conversion efficiency, the modulated output, which consists of the carrier and both sidebands, is optically collimated through a Fabry–Perot filter and is focused onto a room temperature HgCdTe photodetector. A typical detector output is shown in Fig. 6, which displays the spectra of the modulated laser output. One free-spectral-range of the Fabry–Perot is set at approximately 50 GHz. At the laser power level for the experiment, the detector was calibrated to assure that the detected output was not saturated. The peak height of the sideband P_s measured from the shoulder of the carrier is obtained, for a waveguide modulator with a total thickness of 21 μ m, at different microwave frequencies in the range from 12 to 18 GHz. The ratio of P_s to the peak height of the transmitted carrier power P_c at a constant driver power of 20 W is plotted in Fig. 7, as a function of microwave frequency. Over the entire frequency range of 6 GHz, the variation in sideband power is less than 1.7 dB. Optical transmission for this waveguide modulator is 0.32.

Similar measurements were carried out for a modulator with a thickness of 25 μm, rather than the 21 μm device described above and has a similar profile. The highest sideband power conversion for a 25 μm thick waveguide modulator providing 42 percent optical transmission is 0.66 percent at a driver power of 20 W.

The sideband conversion efficiency for these two modulators per one watt microwave drive power at 14 GHz is approximately the same, -39 dB/W (see Table 2), when both the optical and microwave insertion losses are taken into account.

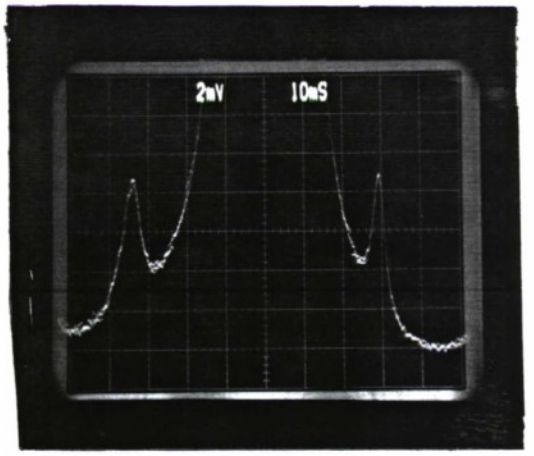

Figure 6. The Spectra of Modulated Laser Output. The Modulator Driver Power is 23.7 W at 13 GHz.

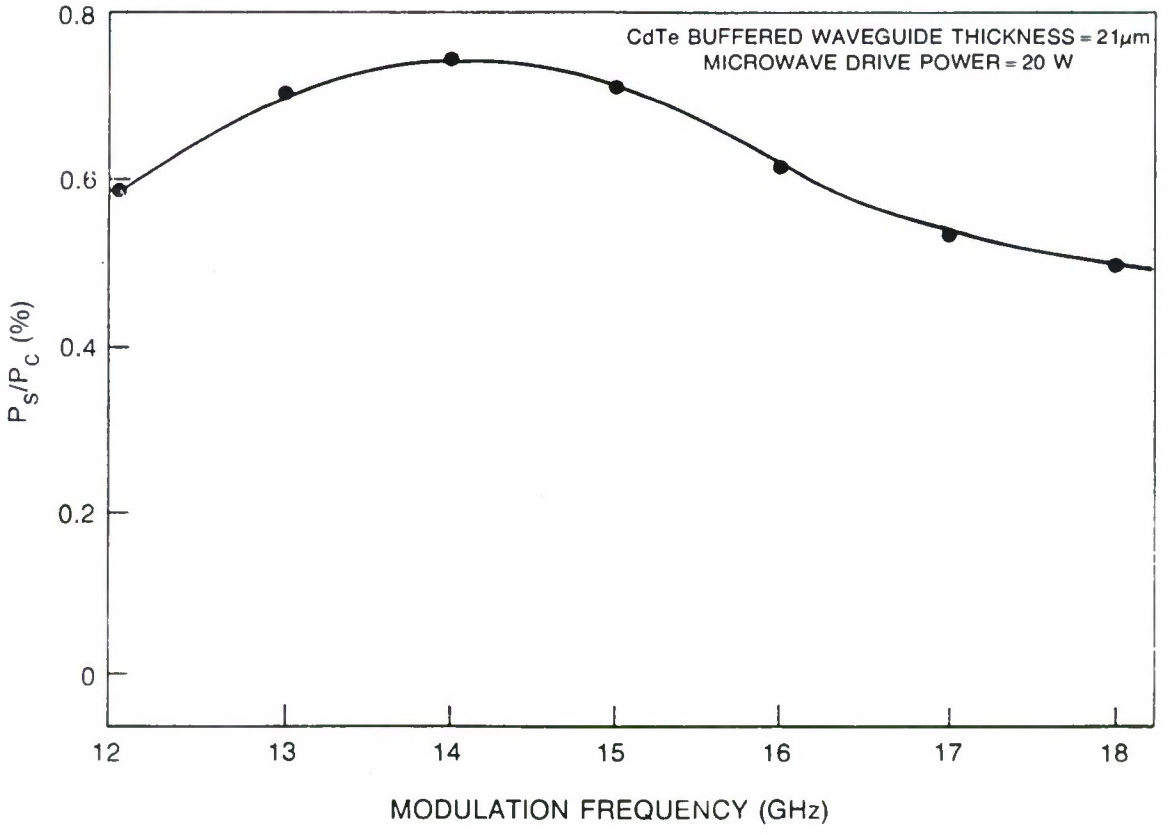

Figure 7. Percent Sideband Power Conversion vs Modulation Frequency

TABLE 2 - SIDEBAND CONVERSION EFFICIENCY OF CdTe BUFFERED WAVEGUIDE MODULATORS

Thickness (μm)	T (%)	Sideband Conversion at 14 GHz (dB)
21	32	-39.2/W
25	42	-38.6/W

CO_2 laser powers as high as 10 watts (CW) and microwave drive powers as high as 35 watts (CW) or 100 Watts (peak at PRF = 1 KHz and a pulsewidth of 10 μ-sec) have been applied to CdTe buffered GaAs waveguide modulators without causing damage. At the above power levels, sideband powers as high as 48.5 mW (CW) or 138.6 mW (pulsed) can be obtained (see Table 3) from the delivered device.

TABLE 3 - SIDEBAND POWER GENERATION

Input Power (W)		Sideband Power
Laser	Microwave	(mW)
10	20 (CW)	27.7
10	35 (CW)	48.5
10	100 (Pulsed)	138.6

2.5 Output Beam Profile

To use the waveguide modulator as a broadband frequency shifter for the local oscillator of the 10.6 μm laser radar receiver, it is imperative that the modulated laser beam profile be of good quality. The laser beam quality emerging from the modulator is strongly dependent on the integrity of the planar waveguide device in terms of the flatness (or the thickness uniformity) the stress-induced birefringence, and material defects. Under this contract, a substantial effort has been devoted to improving the buffered waveguide quality with appropriate fabrication techniques and well characterized materials. A significant improvement in device integrity has been achieved. As a result, the output laser beam not only has more power, compared to the NASA modulator mentioned previously, but also has a much improved beam profile. Because of the inherent nature of prism coupling, there exists a slight asymmetry in the far field beam scan along the length of the coupler (x-scan). Along the width of the microstrip electrode (y-scan), the beam profile remains reasonably symmetric and can be fitted fairly well by a Gaussian. Consequently, the beam shape is slightly elliptical. The output beam has been analyzed by making x and y scans of the beam profile at distances 10 cm (Fig. 8), 70 cm (Fig. 9) and 140 cm (Fig. 10) away from the output prism coupler.

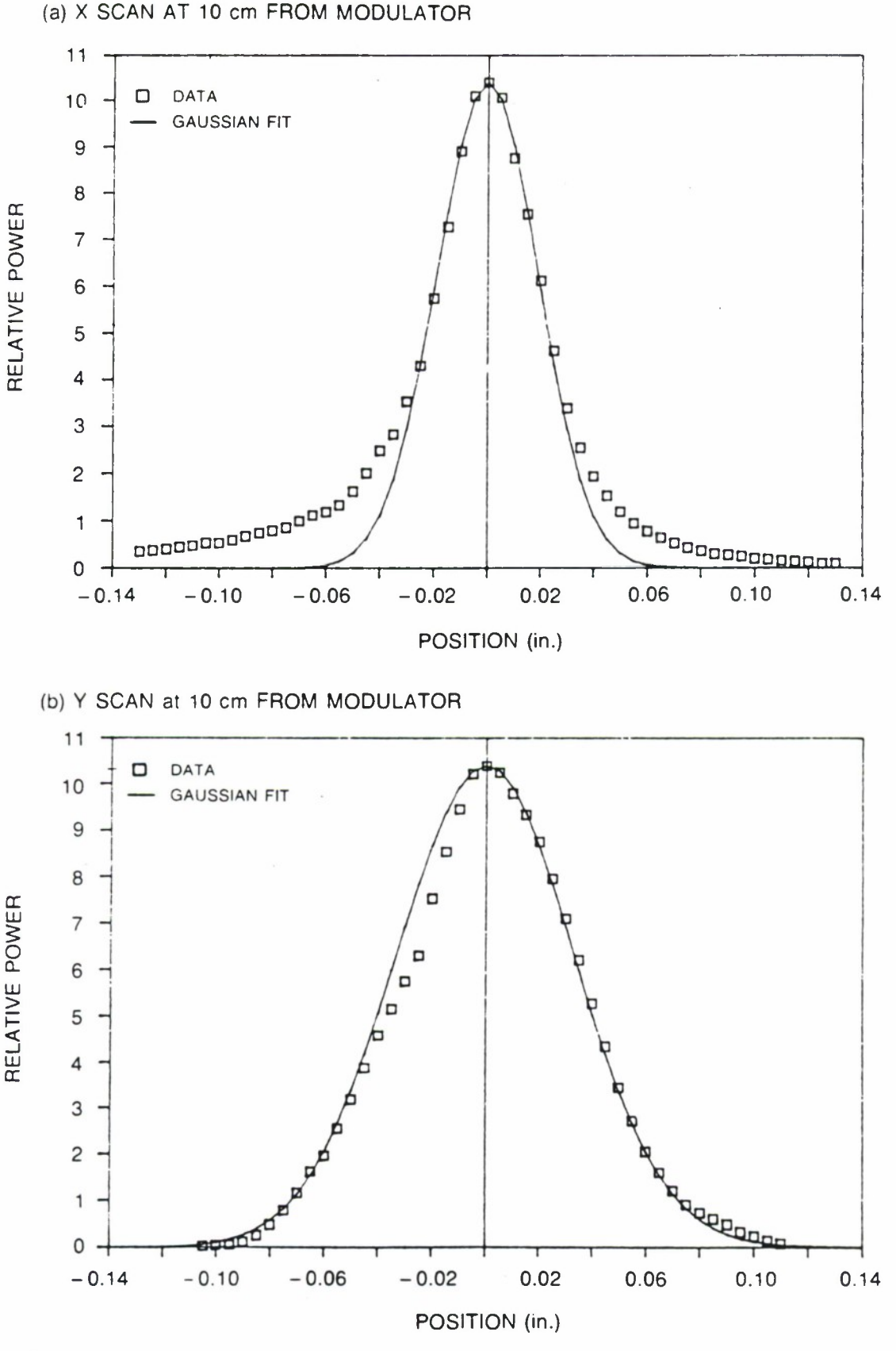

Figure 8. Output Beam Profiles

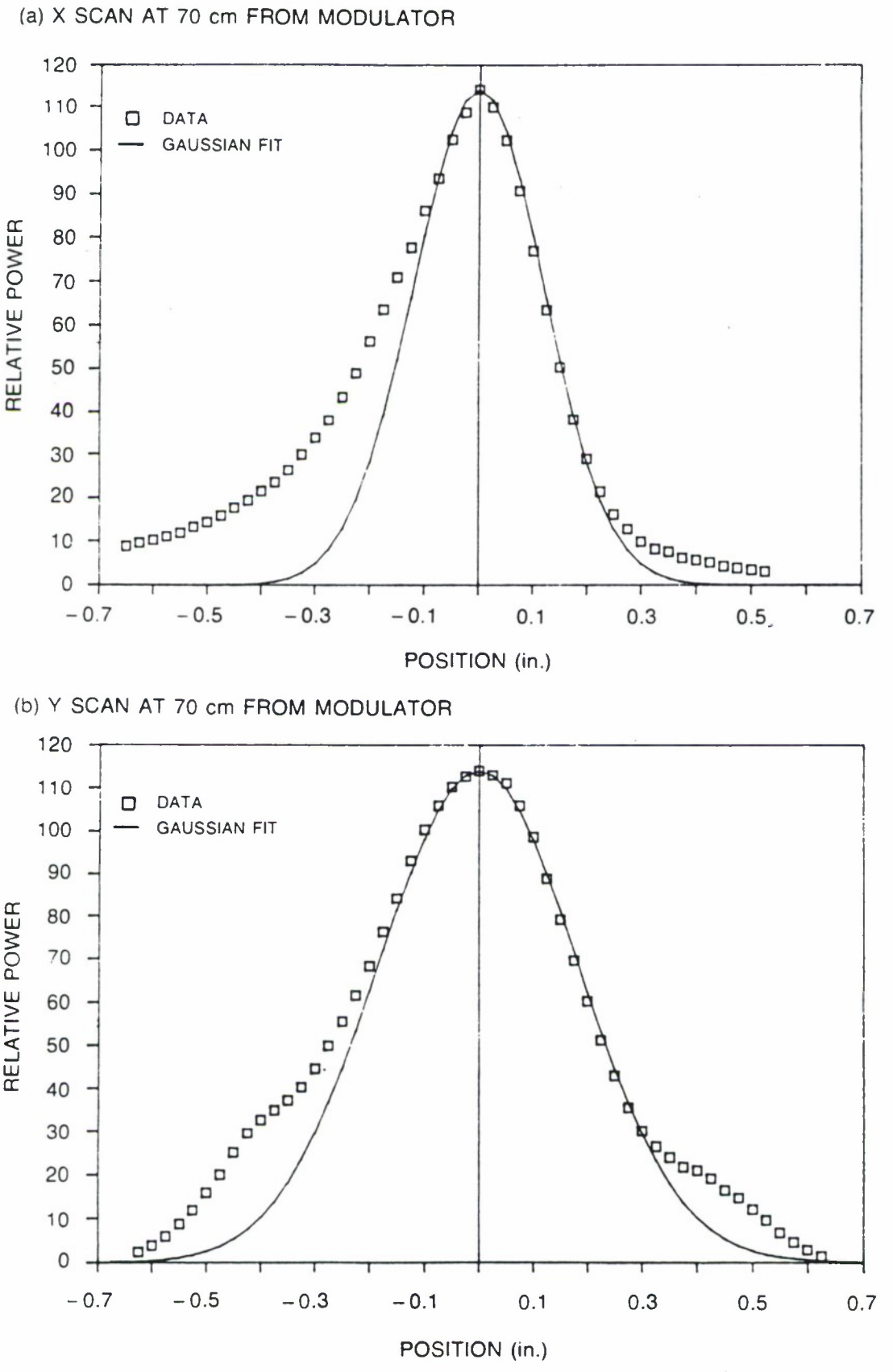

Figure 9. Output Beam Profiles

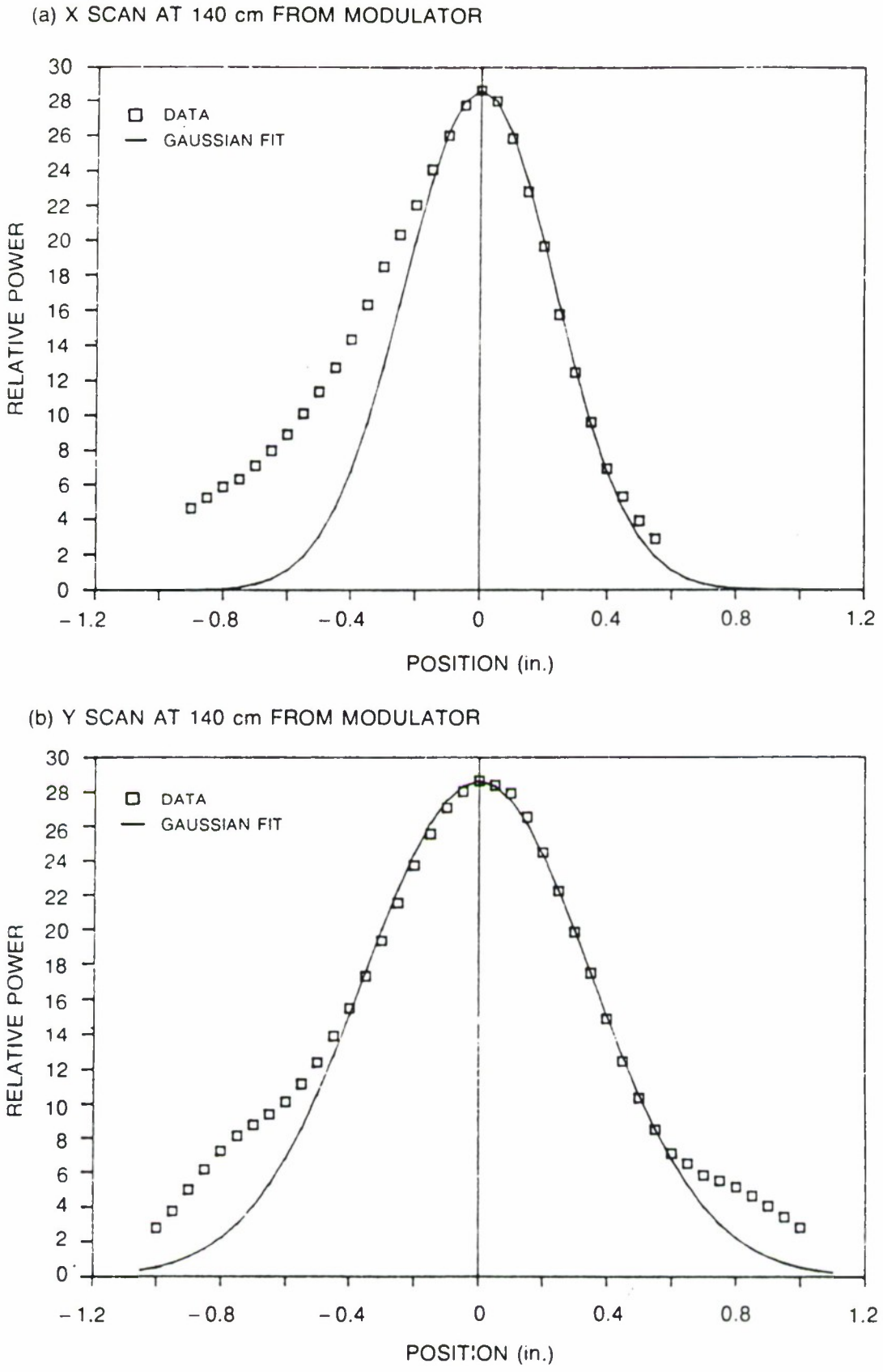

Figure 10. Output Beam Profiles

The full widths at half maximum power (FWHM) measured at three different distances for both x and y scans are plotted in Fig. 11. The results indicate that the output beam shape remains elliptical with no apparent astigmatism, therefore, it can easily be corrected by a simple cylindrical lens. The ratio between the major and the minor axes of the ellipse is approximately 1.2 (see Fig. 11).

2.6 Waveguide Modulator Assembly

Figure 12 shows an assembled modulator, which has been delivered to Lincoln Laboratory. The modulator is located in the housing, which is attached to a chill plate. The focused CO_2 laser beam is incident on the surface of the Ge prism (see Fig. 13) through an entrance hole, at an angle of approximately 85° with respect to the plane of the waveguide. The modulated beam emerges from the output port (see Fig. 12) at the same angle as the input. The transmitted power is critically dependent on the alignment of the modulator with respect to the beam and on the prism loading, which can be controlled by adjusting the screws as shown in Fig. 13. The modulator housing is mounted on a platform (see Fig. 12) which provides 6 degrees of freedom, namely, x, y, z linear adjustments and three angular adjustments. The microwave power can be launched into the modulator through a standard microwave connector located near the input prism coupler. The microwave output must be terminated in a 50 Ω load.

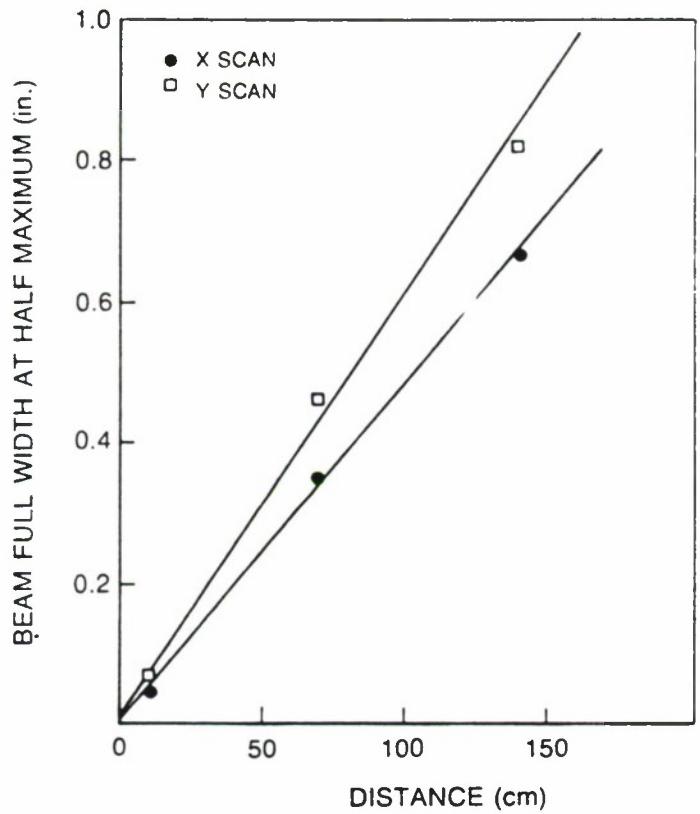

Figure 11. **Plot of the Beam Width (FWHM) as a Function of the Distance Measured From the Output Prism Coupler**

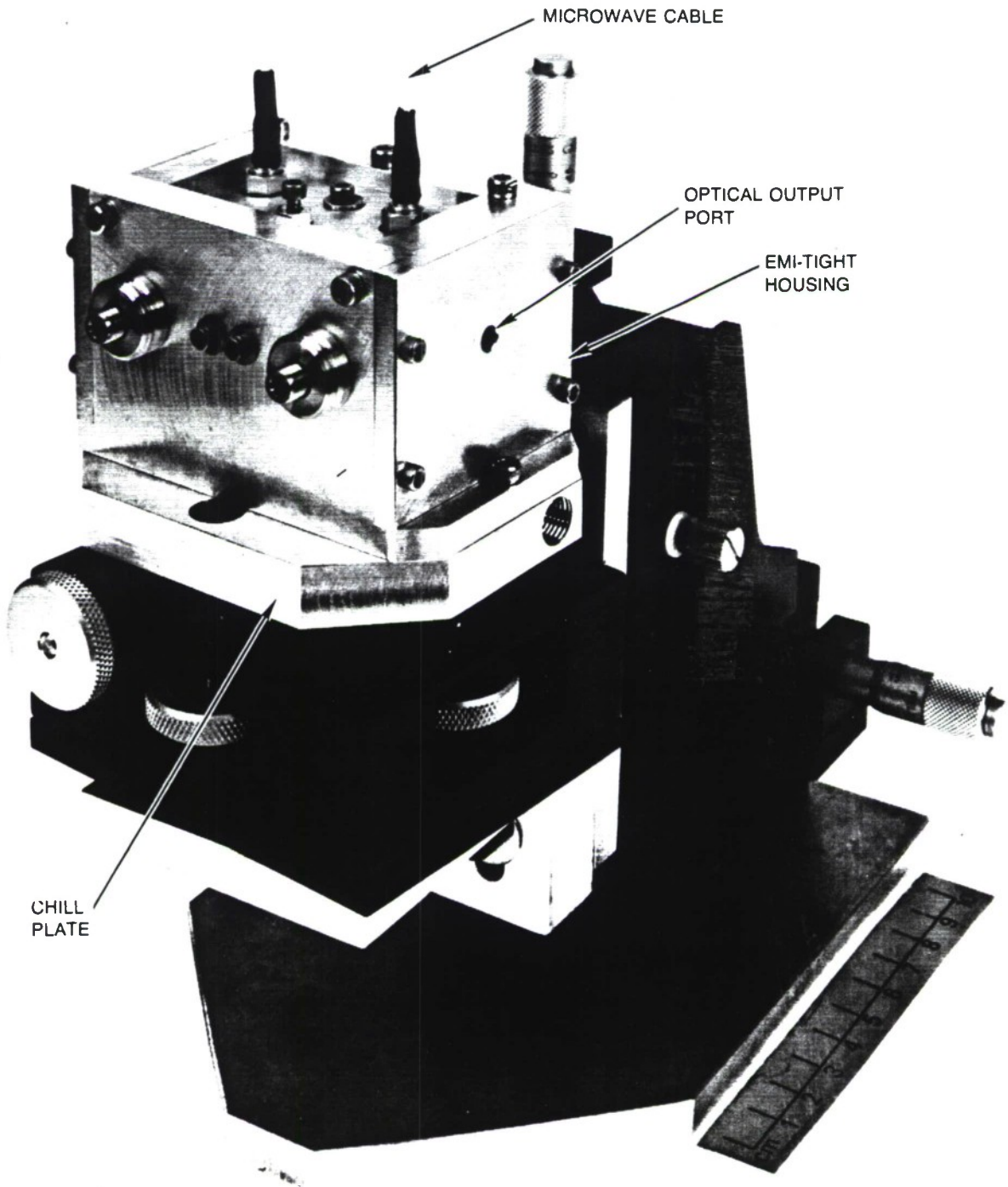

Figure 12. Assembled Modulator

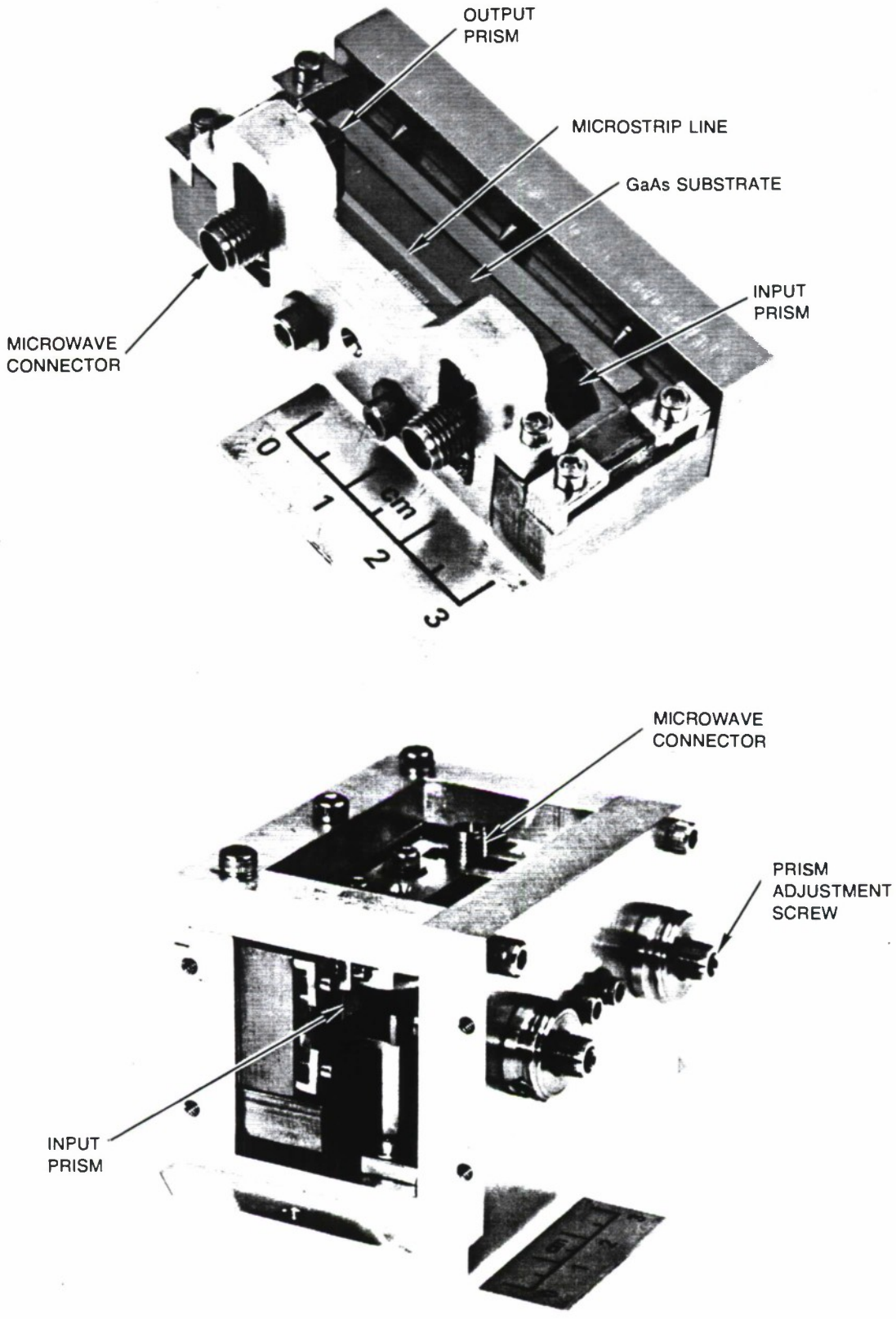

Figure 13. Traveling-Wave Double-Sideband GaAs Modulator Sub-Assemblies

3.0 – DESIGN AND PERFORMANCE EVALUATION OF A T/R FILTER

3.1 Design Considerations

The effect of the filter on both the amplitude and phase of the transmitted and reflected signals is examined. Figure 14 depicts the optical fields of the incident, reflected, and transmitted signals, $\tilde{A}_i$, $\tilde{A}_r$, and $\tilde{A}_t$, which can be represented by expressions of the form

$$\tilde{A} = A_o \exp(j\omega t), \tag{1}$$

where A_o is the optical field amplitude, and ω is the optical radian frequency. In general, we can express the effects of the filter in terms of its transmission and reflection transfer functions as

$$\tilde{A}_t = \tilde{H}_t(\omega)\, \tilde{A}_i, \tag{2}$$

and

$$\tilde{A}_r = \tilde{H}_r(\omega)\, \tilde{A}_i, \tag{3}$$

where, as indicated, $\tilde{H}_t$ and $\tilde{H}_r$ are functions of ω and can be expressed as

$$\tilde{H}_t = |\tilde{H}_t| \exp(j\theta_t), \tag{4}$$

and

$$\tilde{H}_r = |\tilde{H}_r| \exp(j\theta_r), \tag{5}$$

with $|\tilde{H}_t|, \theta_t, |\tilde{H}_r|$, and θ_r being functions of ω.

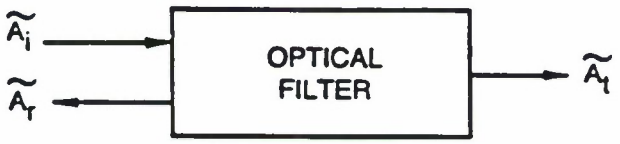

Figure 14. Generalized Optical Filter.

Thus,

$$\bar{A}_t = |\bar{H}_t| A_o \exp\,[j(\omega t + \theta_t)], \tag{6}$$

and

$$\bar{A}_r = |\bar{H}_r| A_o \exp[j(\omega t + \theta_t)]. \tag{7}$$

The filter imposes a change in the amplitude through $|\bar{H}_t|$ and $|\bar{H}_r|$ and a change in phase through θ_t and θ_r.

It is of interest to consider the special case of a phase shift θ_t which is linearly proportional to ω,

$$\theta_t = k_t \omega, \tag{8}$$

with k_t being a constant. Then,

$$\bar{A}_t = |\bar{H}_t|\ A_o \exp[j\omega(t + k_t)]. \tag{9}$$

A linear phase shift can thus be viewed as a simple time delay, which, for many cases of interest, does not degrade the system performance.

For a filter designed to produce minimum distortion over a given frequency band, the specifications for the filter can therefore be expressed as a maximum variation of $|\bar{H}|$ (in dB) and a maximum departure of θ from linear (in deg) over the band.

For comparison with standard filter formulas, the quantities $\bar{H}_t$ and $\bar{H}_r$ can be related to the optical power transmission and reflection coefficients T and R by the expressions

$$T = \frac{I_t}{I_i} = \frac{\bar{A}_t \bar{A}_t^*}{\bar{A}_i \bar{A}_i^*} = \left[\frac{\bar{A}_t}{\bar{A}_i}\right]\left[\frac{\bar{A}_t}{\bar{A}_i}\right]^* = \bar{H}_t\, \bar{H}_t^* = |\bar{H}_t|^2, \tag{10}$$

and

$$R = \frac{I_r}{I_i} = \bar{H}_r\, \bar{H}_r^* = |\bar{H}_r|^2. \tag{11}$$

For a lossless etalon, R is equal to 1-T.

3.2 Fabry–Perot Filter

Referring to Fig. 15, the transfer functions for a Fabry–perot filter can be expressed as [6]

$$\tilde{H}_r = \frac{\tilde{A}_r}{\tilde{A}_i} = \frac{[1-\exp(j\delta)][R]^{1/2}}{1-R\ \exp\ (j\delta)}, \tag{12}$$

and

$$\tilde{H}_t = \frac{\tilde{A}_t}{\tilde{A}_i} = \frac{1-R}{1-R\exp(j\delta)}, \tag{13}$$

where, for an air-spaced etalon,

$$\delta = \frac{4\ \pi\ m\ \ell}{\lambda}\ (m = 1, 2, 3, ...), \tag{14}$$

where ℓ is the etalon spacing and R is the power reflectivity of the etalon mirrors.

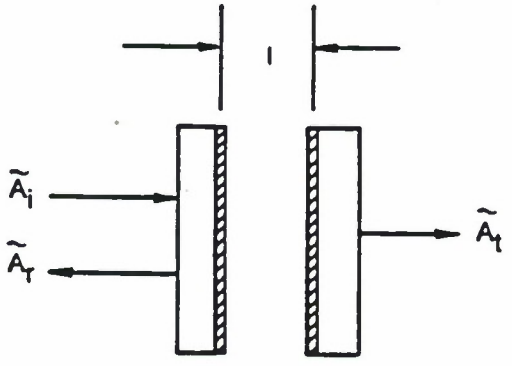

Figure 15. Fabry–Perot Optical Filter.

Using the above expressions, we obtain

$$T = \tilde{H}_t \, \tilde{H}_t^* = \frac{(1-R)^2}{(1-R)^2 + 4R\sin^2(\delta/2)}, \tag{15}$$

$$\theta_t = \tan^{-1}\left[\frac{\mathrm{Im}(\tilde{H}_t)}{\mathrm{Re}(\tilde{H}_t)}\right] = \tan^{-1}\left[\frac{R\sin\delta}{1-R\cos\delta}\right], \tag{16}$$

and

$$\theta_r = \tan^{-1}\left[\frac{\mathrm{Im}(\tilde{H}_r)}{\mathrm{Re}(\tilde{H}_r)}\right] = \tan^{-1}\left[\frac{-(1-R)\sin\delta}{(1+R)(1-\cos\delta)}\right]. \tag{17}$$

The free spectral range Δf is related to the etalon spacing by the usual relation (Ref. 6)

$$\Delta f = f_{m+1} - f_m = \frac{c}{2\ell} \tag{18}$$

For comparison with standard Fabry–Perot curves (e.g., Ref. 6), it is useful to define the etalon finesse as

$$F = \frac{\pi[R]^{1/2}}{1-R} \quad . \tag{19}$$

Plots of T, θ_t, and θ_r for a free spectral range of 30 GHz and for a finesse F of 8.6 are shown in Figs. 16, 17, and 18. From these figures, it may be seen that in the vicinity of the transmission notch, there is a strong variation of amplitude and phase of the transmitted signal. However, in the region mid-way between the transmission peaks, the variation in the transmitted signal amplitude (and hence in the reflected signal amplitude) and the departure of the reflected phase angle from a linear variation are both small.

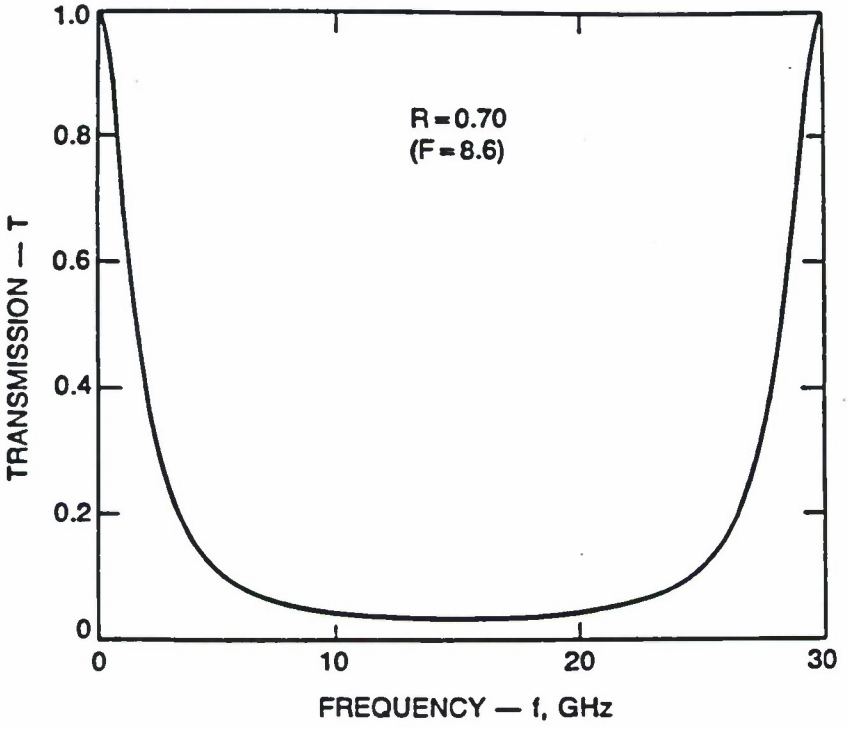

Figure 16. Transmission Coefficient.

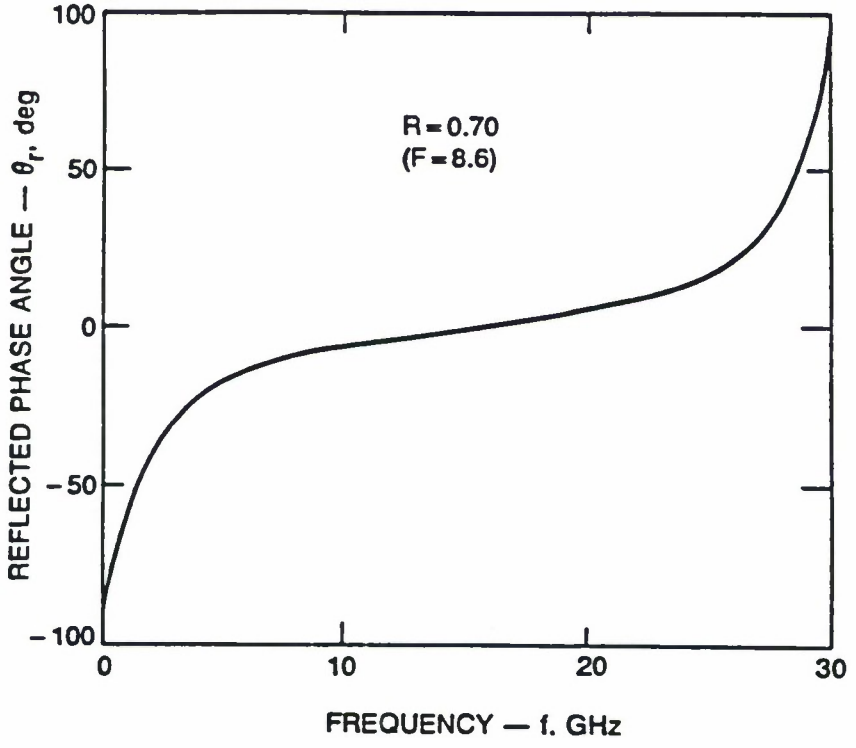

Figure 17. Reflected Phase Angle.

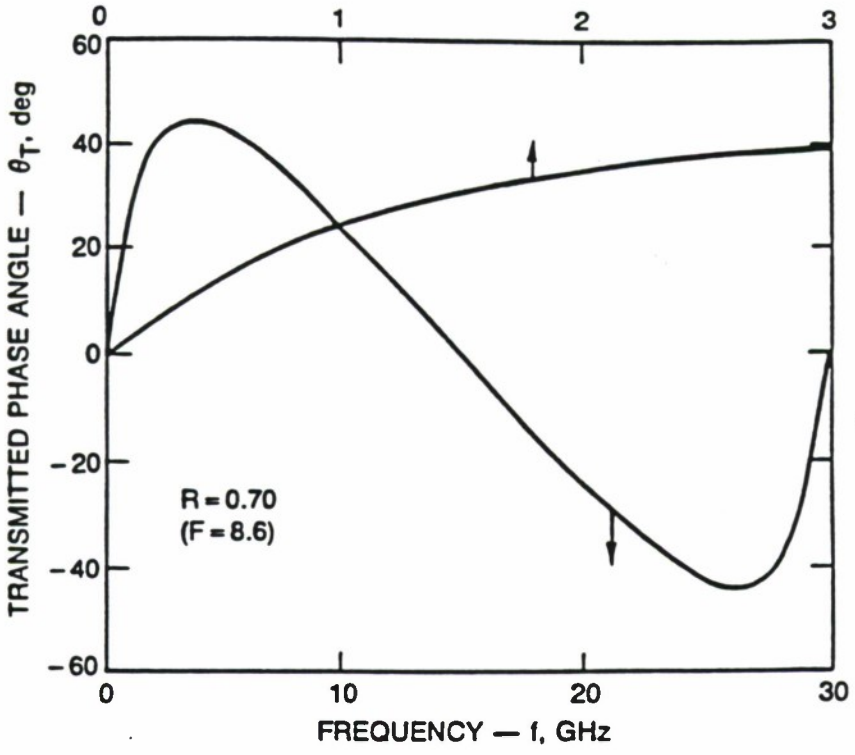

Figure 18. Transmitted Phase Angle.

3.3 Reflective-Mode Fabry-Perot Filter

Based on the above considerations, we have investigated the filter design shown schematically in Fig. 19.

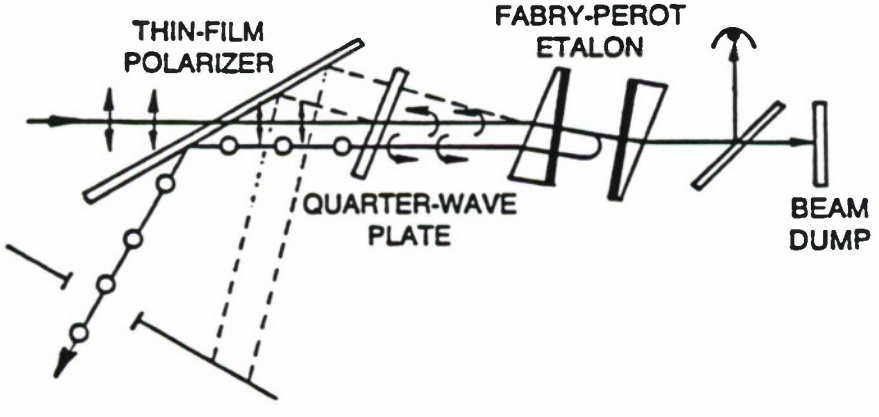

Figure 19. Reflective-Mode Fabry-Perot Filter.

The filter consists of reflective-mode Fabry-Perot etalon in conjunction with an optical duplexer. The duplexer is a thin-film polarizer together with a quarter-wave plate. In order to eliminate reflected signals from the AR-coated etalon mirror surfaces, the mirrors were intentionally wedged, as shown in Fig. 19. Also, a very tight flatness requirement was imposed on the etalon mirrors and a relatively low mirror reflectivity was used in order to maximize the net on-notch throughput. Plots of representative Fabry-Perot throughputs (Ref. 7) are shown in Fig. 20.

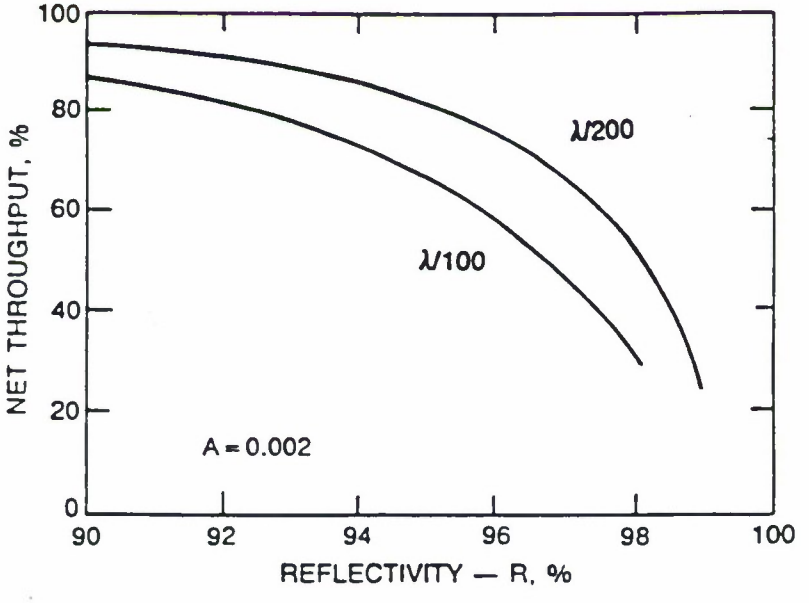

Figure 20. Effect of Mirror Surface Figure On Net Fabry-Perot Throughput.

In order to compensate for slow thermal drifts in the etalon structure, the a. c. dither loop shown in Fig. 21 was used.

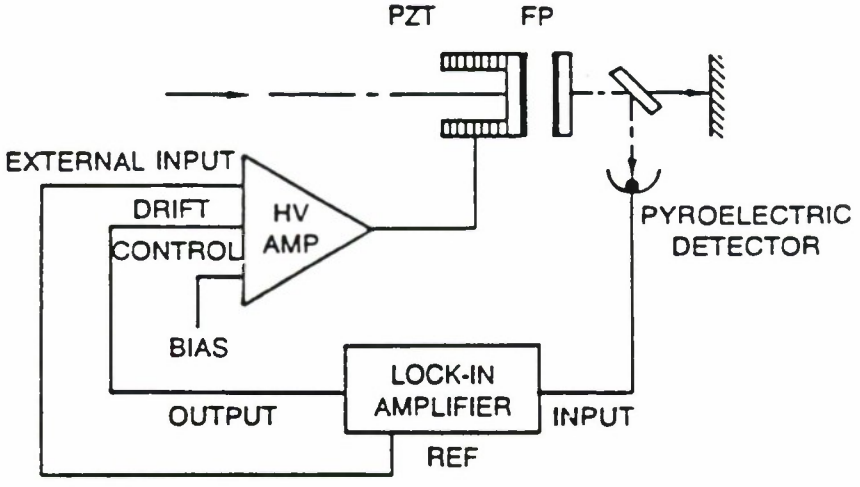

Figure 21. Etalon Locking Loop.

3.4 Experimental Results

Typical experimental results are summarized in Fig. 22 and in Table IV.

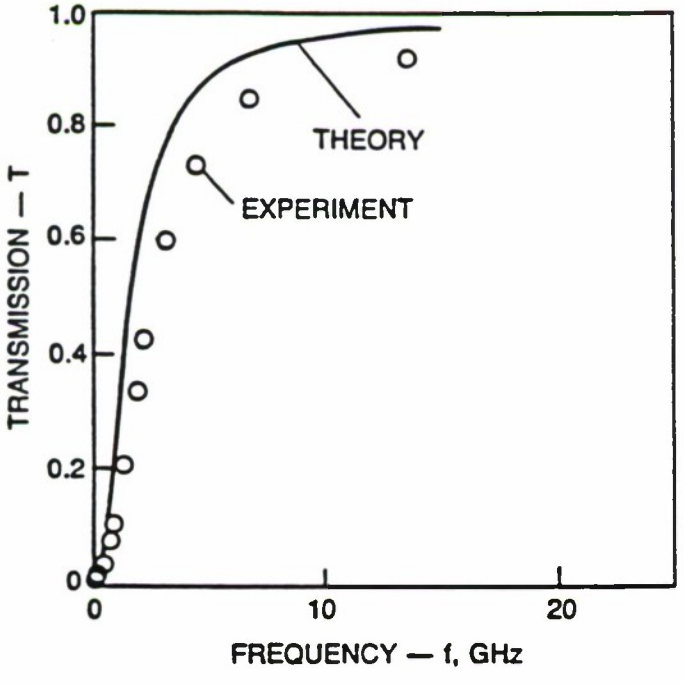

Figure 22. Filter Transmission Coefficient.

TABLE IV – MEASURED FILTER CHARACTERISTICS

Laser input power	2.0 W
Laser line	CO_2 10P(20)
Laser beam diameter	13 mm
Fabry-Perot free spectral range	30 GHz
Fabry-Perot reflectivity	70 %
Fabry-Perot finesse	8.6
On-notch transmitted power	20 mW
Transmitted power 15 GHz off-notch	1.7 W
Rejection (On-notch transmitted power vs. input power accounting for insertion loss)	-19 dB
Insertion loss	0.7 dB

The filter transmission is in reasonable agreement with theory. The finite value of on-notch power from the output port of the filter (corresponding to a rejection ratio of ~ 20 dB) was probably due to mirror surface error and to aberrations in the optical beam. The measured rejection ratio of -19 dB is adequate for many applications and indicates that the present filter design represents an effective and relatively simple method for removing the unwanted carrier signal from the output of a double sideband modulator.

REFERENCES

1. P. K. Cheo, *Frequency Synthesized and Continuously Tunable IR Laser Source in 9–11 μM*, IEEE J. Quant. Elect. QE-20, 700, 1984.

2. G. W. Sachse, *Microwave Tunable Laser Source: A Stable, Precision Tunable Heterodyne LO*, Int. Conf. on Heterodyne Systems and Technology, Williamsburg, VA, 1980.

3. R. Eng, and S. Davidson, *The Conversion Efficiency of an Unbuffered GaAs Microstrip Electro-Optic Modulator: Theoretical and Experimental Results*. Lincoln Lab. Project Memorandum 52PM-ODT-0032, 22 March, 1989.

4. UTRC R87-927477, *Design Studies of 10 Micron Laser Radar Modulators*, Final Technical Report, January, 1988.

5. P. K. Tien and R. Ulrich, J. Opt. Soc. Am., 60, 1325, 1970.

6. A. Yariv, *Optical Electronics*, 3rd Ed., Holt, Rinehart and Winston, N.Y., 1985.

7. Burleigh Technical Note.

REPORT DOCUMENTATION PAGE

Form Approved
OMB No. 0704-0188

1. AGENCY USE ONLY *(Leave blank)*	2. REPORT DATE	3. REPORT TYPE AND DATES COVERED
	July 1989	

4. TITLE AND SUBTITLE

CdTe Buffered GaAs Thin-Slab IR Waveguide Modulators and T/R Filter

5. FUNDING NUMBERS

F19628-85-C-0002
P.O. BX-1404

6. AUTHOR(S)

P.K. Cheo, R.T. Brown, G. Carrier, W. Glueck, R. Wagner, and M. Gilden

7. PERFORMING ORGANIZATION NAME(S) AND ADDRESS(ES)

United Technologies Research Center
East Hartford, CT 06108

8. PERFORMING ORGANIZATION REPORT NUMBER

R89-927784

9. SPONSORING/MONITORING AGENCY NAME(S) AND ADDRESS(ES)

Lincoln Laboratory, MIT
P.O. Box 73
Lexington, MA 02173-9108

10. SPONSORING/MONITORING AGENCY REPORT NUMBER

ESD-TR-89-222

11. SUPPLEMENTARY NOTES

None

12a. DISTRIBUTION/AVAILABILITY STATEMENT

Approved for public release; distribution is unlimited.

12b. DISTRIBUTION CODE

13. ABSTRACT *(Maximum 200 words)*

CdTe buffered GaAs thin-slab waveguide modulators with very low optical and microwave insertion losses have been fabricated. The measured single sideband power that can be converted from the CO_2 laser input power is -39 dB for one watt microwave driver power, as compared to a measured value of -44 dB from an unbuffered modulator. The output quality has also been improved significantly.

A transmission/reflection filter designed to separate the sidebands from the carrier has been fabricated and tested. The rejection ratio of carrier power to sideband power is -19 dB.

14. SUBJECT TERMS

electro-optic modulator
GaAs modulators
traveling wave electro-optic modulator
infrared integrated optics
microwave-optical interactions

15. NUMBER OF PAGES
33

16. PRICE CODE

17. SECURITY CLASSIFICATION OF REPORT	18. SECURITY CLASSIFICATION OF THIS PAGE	19. SECURITY CLASSIFICATION OF ABSTRACT	20. LIMITATION OF ABSTRACT
Unclassified	Unclassified	Unclassified	